Coded excitation waveform engineering for high frame rate synthetic aperture ultrasound imaging

Bahman Lashkari *, Kaicheng Zhang, Edem Dovlo, Andreas Mandelis

Center for Advanced Diffusion-Wave and Photoacoustic Technologies (CADIPT), Department of Mechanical and Industrial Engineering, University of Toronto, Toronto M5S 3G8, Canada

ARTICLE INFO

ABSTRACT

Coded excitation was initially introduced to ultrasound imaging as a method for enhancing the signal-to-noise ratio (SNR). However, this method was also shown to be helpful in conjunction with synthetic aperture transmission for high frame rate imaging. Recently, we introduced two families of mismatched coded excitations based on frequency modulation chirp and combined frequency modulation and Golay code. Here "mismatched" indicates that the coded excitations generate very small cross-correlations among themselves while each has a very strong autocorrelation. Employing weakly correlated coded excitations enables performing simultaneous insonifications from several elements of the ultrasonic transducer and receiving distinguishable responses to each code. In this work, we propose and experimentally demonstrate another set of mismatched correlated coded excitations based on Golay codes. The generated phase codes share identical duration and center frequency which results in similar SNR and image resolution.

1. Introduction

Ultrasound (US) has become a widespread medical tool with capabilities more than just imaging. Velocity and flow measurements, elastography, therapeutic ultrasound, as well as 3D imaging, are just among the many features of ultrasound modalities [1]. High frame rate is a fundamental requirement for some of the ultrasound cutting edge features such as 3D imaging or real-time video recording. Low-speed signal acquisition, on the other hand, causes cluttering in the images and error in blood velocity estimations. The increase in the speed of US imaging systems not only facilitates real-time 3D imaging, but can also be used to increase the 2D image quality at the normal frame rate.

Various approaches have been proposed to achieve high-frame-rate imaging while preserving image quality. Parallel beamforming or multi-line transmission (MLT) is a method based on generating a spherical wave by transmitting a diverging beam from multiple elements, which is also called "explososcan" [2–4]. Similarly, there have been attempts to perform fast volumetric ultrasound imaging by multiple beams [5]. The complexity of those systems was fairly high, however, they enabled 3D imaging. Parallel beamforming can also be used to generate a plane wave beam. Plane-wave compounding is shown to be an effective method for high-frame-rate imaging [6,7]. Another promising method is multiple-element synthetic aperture imaging (SAI) which can increase the frame rate while reducing system complexity [8–11]. The performance of SAI has been compared with parallel beamforming in a few recent publications [12,13].

Many different techniques have been employed to perform multiple transmissions in the SAI method. Most of these methods generate and benefit from mismatched coded excitation (CE) waveforms. One common technique was based on choosing long independent Golay codes (GC) or m-sequences, to minimize the cross-correlation (CC) between the signals [14,15]. Alternatively, it was shown that, by employing the equivalence properties of GCs [16], a set of GCs can be generated in a way that while their

CCs are nonzero, the summation of CCs of complementary codes cancels each other out [17,18]. The other techniques employ the Hadamard decoding method [19] or a combination of Hadamard decoding and dissimilar GCs [20]. Hadamard decoding has been widely used to generate orthogonal codes with GCs and even with chirps [21,22]. Another approach is to use a Hadamard matrix to encode the transmitted pulses based on their delay in transmission [23].

Various methods have been suggested to generate mismatched codes with frequency modulation (FM) signals as well. Frequency sweeps with dissimilar slopes yield mismatched codes. Two FM chirps with similar duration and bandwidth but opposite slopes generate a very effective set of mismatched codes, however the method is limited to two codes only [22]. Use of different durations or different portions of the bandwidth can result in an arbitrary number of mismatched codes but with non-uniform signal-to-noise ratios (SNR) and resolutions [24]. Alternatively, the bandwidth can be divided into several parts, so that multiple excitation signals cover different parts of the bandwidth. The excitations can be single frequency waveforms or chirps [25–28]. The combination of frequency spectrum division and opposite slopes has also been proposed to generate multiple focal points by simultaneous multiple transmissions [29].

In our previous work [30], we proposed two methods for generating arbitrary numbers of mismatched codes with identical durations and bandwidths. The first method is applicable to FM signals. We showed that by dividing the signal duration into two or more parts and sweeping the bandwidth with different slopes, multiple mismatched codes can be generated. Another family of mismatched CEs are generated by combining GC and FM signals. The carrier waveform convolved with GCs is replaced by an FM signal. The different number of bits in different GCs induces different durations for FM signals, thus each code is uncorrelated with other codes due to their different slopes of carrier FM signals. The correlation between different parts of the same code is cancelled out by the sidelobe eliminating property of GC. In this work we present a new family of mismatched CEs based on GCs. The goal is to generate uncorrelated CEs with similar signal duration and center frequency (CF).

2. Method

2.1. Mismatched coded excitation for ultrasound imaging

CE is an established technique in radar technology. A variety of encoding signals has been proposed and tested [31]. The limited bandwidth of the ultrasonic transducer and acoustic attenuation are the major factors that curb the achievable gain in SNR when using CE in ultrasound imaging [32]. Although SNR enhancement was the primary motive for using CE in ultrasound imaging, it was shown that CE enables the generation of mismatched codes. This paper proposes and experimentally demonstrates the use of a new family of mismatched CEs with identical duration and CF. The feasibility of ultrasound imaging with these new CEs is compared with the method introduced in our previous work based on mismatched FM chirps [30]. Those mismatched CEs are generated by allocating FM chirps with different slopes in the same transmitted code. Fig. 1(a) shows a set of frequency sweeps and a sample FM code. All the generated codes share the same bandwidth. The key condition, however, is that the slopes of the sweeps in different codes, as well as different parts of each code, should be dissimilar. It was proven that the CC between two frequency sweeps with different slopes and identical bandwidth is inversely proportional to the bandwidth and duration difference between the two slopes [33]. Additionally, the CC is also related to the
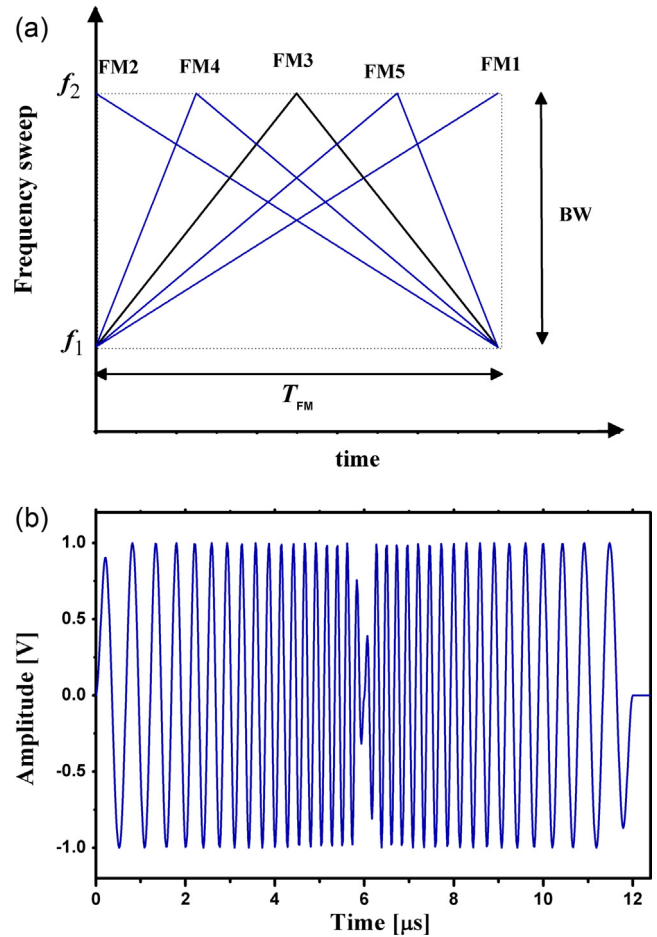
Fig. 1. (a) Frequency sweeps with identical bandwidth (BW) and duration, generating mismatched frequency modulations (FM). (b) Waveform based on FM3, the frequency first sweep up from 1.3 to 4.7 MHz and then sweep down from 4.7 to 1.3 with different slope (10% tapering has been applied on each frequency sweep part).

duration of both frequency sweeps as well [30]. Therefore, FM1 to FM5 in Fig. 1(a) can provide a set of mismatched frequency modulation chirps. FM1 and FM2 are the up and down-chirps employed by several authors [22,24] and FM3 to FM5 are generated with the proposed method [30].

2.2. The new family of mismatched coded excitations based on Golay codes

Here, we propose a new method of generating mismatched CEs employing binary sequences. Complementary GCs are used to generate a family of uncorrelated excitation signals. GCs generate auto-correlations proportional to their lengths. A set of complementary GC binary sequences with length N, such as A(k) (k = 0, 1, . . . , N−1) and B(k) satisfies:

$$A(k) * A(-k) + B(k) * B(-k) = 2N\delta(k) \tag{1}$$

where * represents convolution and $\delta(k)$ represents the Dirac delta function. There can be multiple distinct GCs with similar length. The difficulty is that any two GCs can have large CC between themselves [24]. As mentioned before, there exist orthogonal GCs with identical length, but no algorithm was suggested for making more than two uncorrelated codes [17,18]. Thus, no attempt is made here to use different GCs with the same length. To ensure identical SNR, the GC design in this work is based on the same duration for all GCs.

Unlike chirps, the duration of GCs is not arbitrary, the reason being that only specific sizes of GCs exist. There are algorithms to generate new codes from known GCs, however, these algorithms either generate a new m × n-bit code from the original m and n-bit codes or generate a (2 × m)-bit code from an original m-bit code [34–36]. The latter algorithm is typically used recursively to generate a $(2^n \times m)$-bit code from an m-bit code. Considering that the frequency is specified by image requirements and transducer CF, there are limited options for GC duration. Another important parameter in using GCs is the carrier waveform. GCs can be convolved with half cycle (HC) or full-cycle (FC) sinusoidal or square waveforms. The selection of carrier waveform affects spectrum, bandwidth, axial resolution and total energy transmitted [36].

The new method is based on concatenating smaller codes (could be identical) with different carrier frequencies to generate a new code with length (duration) and frequency same as the original code. Fig. 2(a) shows a conventional 16-bit GC with 2.73 MHz CF, and Fig. 2(b) shows a code generated by concatenating two 8-bit codes with 4.28 and 2 MHz carrier frequencies. The dashed lines show the complementary code in each case. In Fig. 2(b), since the duration of each part of the code is different, it can be observed that the average frequency of the compound code is not simply the average of frequencies. Although the number of bits for constituent codes is similar, the frequencies are different. Having different frequencies, each part of the compound GC is mismatched with the other part as well as with other GCs. Therefore, the new GCs generate a new family of mismatched GCs. To ensure that these concatenated GCs are generated having the same length as the original GC, discrete time description was adopted which is congruent with the digital signal processing application developed in LabView (NI, USA) platform for this work. It is assumed that the center frequency of the main carrier waveform is f_c, the sampling frequency is f_s, and the number of digitized points describing each bit of the original GC is N_c. Thus, regardless of the carrier waveform (FC or HC, sinusoidal or square), the duration of each GC bit is N_c/f_s. The digitized points defining each bit of two concatenated GCs are selected as $N_c + n$ and $N_c - n$, where n is an integer. Therefore, the durations of two concatenated GCs are $(N_c \pm n)/f_s$, and the associated frequencies are $f_c/(1 \pm n/N_c)$. As seen in Fig. 2(a) and (b), N bits with frequency f_c, generate exactly the same duration as N/2 bits of frequency $f_c/(1 + n/N_c)$ and N/2 bits of frequency $f_c/(1 - n/N_c)$. The total duration of the concatenated GCs is:

$$\frac{N}{2}\frac{N_c + n}{f_s} + \frac{N}{2}\frac{N_c - n}{f_s} = N\frac{N_c}{f_s} \tag{2}$$

Eq. (2) demonstrates how the choice of $f_c/(1 \pm n/N_c)$ frequencies for two parts of the concatenated GC maintain the duration and number of bits of the GC equal to the conventional GC. Table 1 shows the frequencies of five mismatched GCs generated by this method. The duration of the code can be altered by selecting N, the length of the conventional GC with uniform carrier frequency. Here, N/2 is not arbitrary: a GC with length N/2 should exist. Then, using the algorithm for generating longer codes from smaller GCs ensures the existence of GCs with length N. In the presented example (Fig. 2(a) and Table 1), f_s = 30 MHz, and f_c = 2.73 MHz, therefore, N_c = 11. The frequencies of the concatenated GCs are determined for n = 1, 2, 3, and 4 (Fig. 2(b) and Table 1).

2.3. The cross-correlation of concatenated Golay codes

Assuming A(k) and B(k) are the complementary sequences of the N-bit GC and, C(k) and D(k) are the complementary sequences of the ½N-bit GC, the GCs are generated by convolving the carrier waveforms with their corresponding GC sequences. For instance, for a sinusoidal carrier waveform, the conventional GC is:
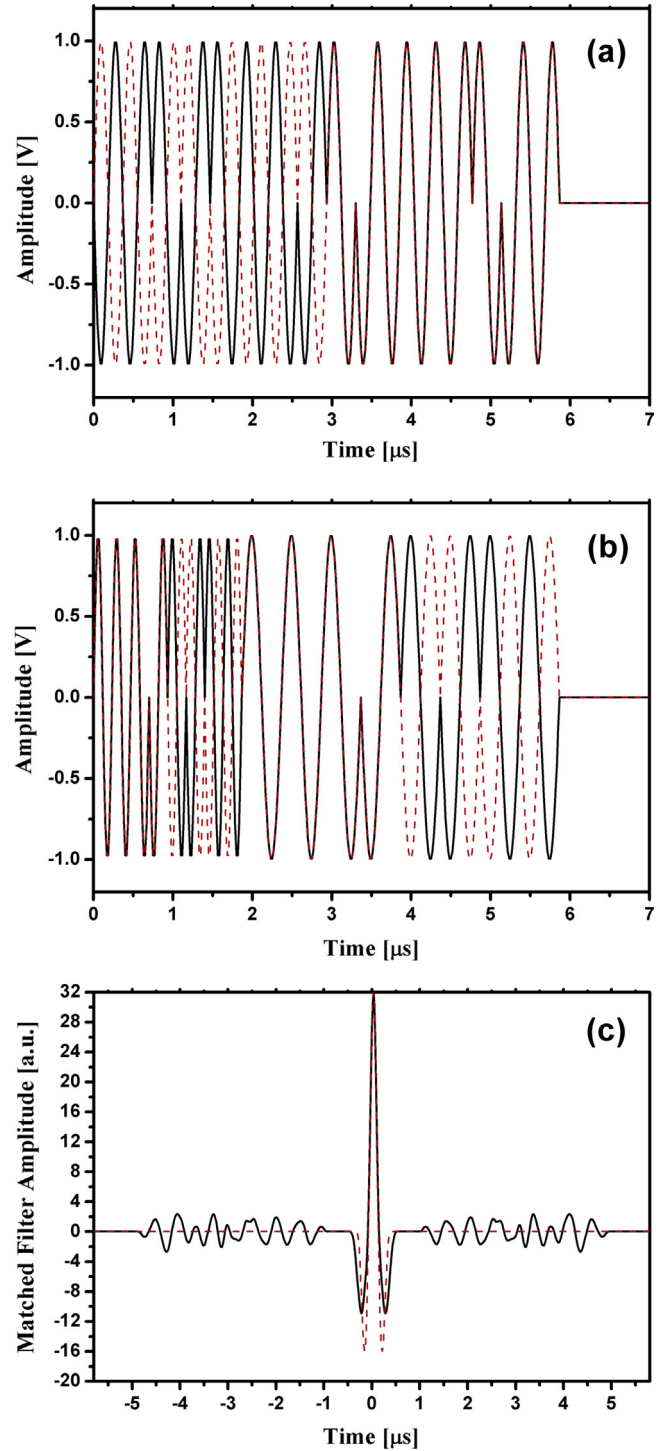
Fig. 2. (a) The original 16-bit FC GC; and (b) a compound GC generated by concatenating two 8-bit FC GCs with different frequencies; the complementary codes in each plot are shown with dashed lines (c) the matched filter output of both GCs in (a) and (b). The matched filtered output of concatenated GC produced sidelobes which do not exist in the output of conventional GC (MSR = −21.5 dB).

$$g_{A1}(t) = \sum_{k=0}^{N-1}\left(A(k)\delta\left(t - \frac{kN_c}{f_s}\right)\right) * \left[\cos(\pi f_c t)rect\left(\frac{f_s t}{N_c}\right)\right] \tag{3a}$$

$$g_{B1}(t) = \sum_{k=0}^{N-1}\left(B(k)\delta\left(t - \frac{kN_c}{f_s}\right)\right) * \left[\cos(\pi f_c t)rect\left(\frac{f_s t}{N_c}\right)\right] \tag{3b}$$

Table 1
The new GCs generated by concatenating a GC with different frequencies. The lengths and frequencies of constituent GCs are shown. (For instance in Fig. 2(a) and (b), N = 16.)

GC #	Length of 1st part [bits]	CF of 1st part [MHz]	Length of 2nd part [bits]	CF of 2nd part [MHz]
GC1	N	2.73	0	0
GC2	N/2	2.5	N/2	3
GC3	N/2	2.3	N/2	3.33
GC4	N/2	2.14	N/2	3.75
GC5	N/2	2	N/2	4.286

The concatenated GCs are described as:

$$g_{Cn}(t) = G_{Cn1}(t) * \left[\cos\left(\frac{\pi f_c t}{1 - n/N_c} \right) rect\left(\frac{f_s t}{N_c - n} \right) \right]$$
$$+ G_{Cn2}(t) * \left[\cos\left(\frac{\pi f_c t}{1 + n/N_c} \right) rect\left(\frac{f_s t}{N_c + n} \right) \right] \tag{4a}$$

$$g_{Dn}(t) = G_{Dn1}(t) * \left[\cos\left(\frac{\pi f_c t}{1 - n/N_c} \right) rect\left(\frac{f_s t}{N_c - n} \right) \right]$$
$$+ G_{Dn2}(t) * \left[\cos\left(\frac{\pi f_c t}{1 + n/N_c} \right) rect\left(\frac{f_s t}{N_c + n} \right) \right] \tag{4b}$$

where

$$G_{Cn1}(t) = \sum_{k=0}^{N/2-1} \left(C(k)\delta\left(t - \frac{k(N_c - n)}{f_s} \right) \right)$$

$$G_{Cn2}(t) = \sum_{k=0}^{N/2-1} \left(C(k)\delta\left(t - \frac{k(N_c + n)}{f_s} - \frac{N(N_c - n)}{2f_s} \right) \right)$$

$$G_{Dn1}(t) = \sum_{k=0}^{N/2-1} \left(D(k)\delta\left(t - \frac{k(N_c - n)}{f_s} \right) \right) \tag{5}$$

$$G_{Dn2}(t) = \sum_{k=0}^{N/2-1} \left(D(k)\delta\left(t - \frac{k(N_c + n)}{f_s} - \frac{N(N_c - n)}{2f_s} \right) \right)$$

$$n = 1, 2, 3, \ldots$$

Eqs. (3) and (4) are useful for both HC and FC carriers. The average frequency of each of these new codes is the same as the original GC (here 2.73 MHz). The same GCs introduced here are used in the simulations and in experiments with different code lengths (N). The matched filtered output of concatenated GC can be calculated similar to a conventional GC:

$$R_{g_n g_n}(t) = g_{Cn}(t) * g_{Cn}(-t) + g_{Dn}(t) * g_{Dn}(-t) \tag{6}$$

The CCs of the carrier waveforms can be calculated as:

$$R_{c, N_c+n}(t) = \left[\cos\left(\frac{\pi f_c t}{1 + n/N_c} \right) rect\left(\frac{f_s t}{N_c + n} \right) \right]$$
$$* \left[\cos\left(\frac{\pi f_c t}{1 + n/N_c} \right) rect\left(\frac{f_s t}{N_c + n} \right) \right] \tag{7a}$$

$$R_{c, N_c-n}(t) = \left[\cos\left(\frac{\pi f_c t}{1 - n/N_c} \right) rect\left(\frac{f_s t}{N_c - n} \right) \right]$$
$$* \left[\cos\left(\frac{\pi f_c t}{1 - n/N_c} \right) rect\left(\frac{f_s t}{N_c - n} \right) \right] \tag{7b}$$

$$R_{c, N_c-n, N_c+n}(t) = \left[\cos\left(\frac{\pi f_c t}{1 - n/N_c} \right) rect\left(\frac{f_s t}{N_c - n} \right) \right]$$
$$* \left[\cos\left(\frac{\pi f_c t}{1 + n/N_c} \right) rect\left(\frac{f_s t}{N_c + n} \right) \right] \tag{7c}$$
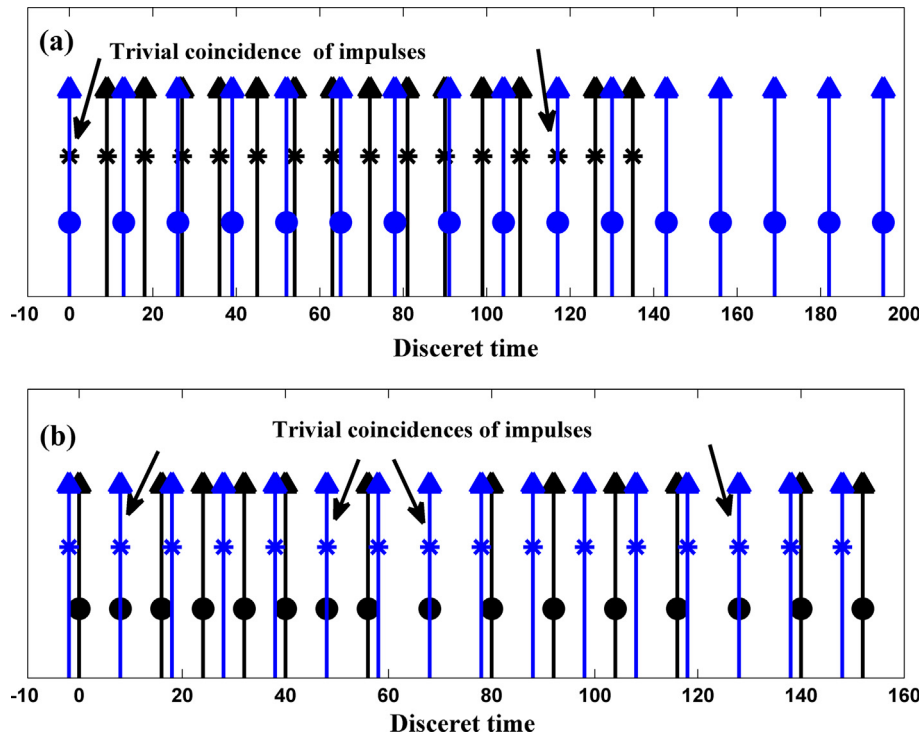
Fig. 3. (a) An example for the coincidences of impulses of two codes (marked with '*' and 'o') with different duration of bits (durations of bits are 9 and 13, (N_c = 11, n = 2), the number of bits for each code is sixteen). (b) An example showing the coincidences of impulses of a concatenated code (with N_c ± n cycle duration and, marked with 'o' in the figure) and impulses of a conventional GC (with N_c cycle duration and, marked with '*' in the figure).

Therefore:

$$R_{g_n g_n}(t) = 2\frac{N}{2}\delta(t) * R_{c,N_c-n} + 2\frac{N}{2}\delta(t) * R_{c,N_c+n}$$
$$+ [G_{Cn1}(t) * G_{Cn2}(-t) + G_{Dn1}(t) * G_{Dn2}(-t)$$
$$+ G_{Cn2}(t) * G_{Cn1}(-t) + G_{Dn2}(t) * G_{Dn1}(-t)] * R_{c,N_c-n,N_c+n} \quad (8)$$

The first two terms are the matched filtered results of two GCs with N/2 bits which generate the same signal enhancement as one GC with N bits. The other four terms generate additional sidelobes on both sides of the main peak. Fig. 2(c) shows the final CC of the GCs shown in Fig. 2(a) and (b). As described in Eq. (6), the autocorrelation of each part of the complementary codes was calculated and then they were added together to generate the final signal. The final CCs of Fig. 2(a) and (b) are shown with dashed line and solid line, respectively.

2.4. Mainlobe-to-sidelobe and autocorrelation to cross-correlation ratio

It can be seen that the concatenated GC generates sidelobes on both sides of the main peak (Fig. 2(c)). To estimate the mainlobe-to-sidelobe ratio (MSR), first we estimate the maximum of each term regardless of carrier waveforms. The maximum occurs when the impulses of G_{Cn1} and G_{Cn2} coincide and have the same sign, therefore the summation generates the maximum unwanted sidelobe. To find the worst case we assume all of the GC coefficients are positive (or negative) and, therefore, they add up. The impulses of G_{Cn1} and G_{Cn2} occur at intervals $(N_c + n)/f_s$ and $(N_c - n)/f_s$. The coincidence of two impulses, one from each code, trivially occurs as a result of cross-correlation process. The possibility of more coincidences depends on whether the kth impulse of the first code occurs at the same time from the starting point as the time the mth impulse of the second code (Fig. 3(a)). Therefore:

$$Max[G_{Cn1}(t) * G_{Cn2}(-t)] \leqslant \left[1 + int\left[\frac{(\frac{N}{2}-1)(N_c-n)}{LCM(N_c-n,N_c+n)}\right]\right]\delta(t-t_i) \quad (9)$$

where LCM is the least common multiple between the two intervals and $int()$ returns the integer value of the number. The number of possible maxima in Eq. (9) can be readily calculated. We assume that the maxima of $G_{Cn1}(t) * G_{Cn2}(-t)$ and $G_{Dn1}(t) * G_{Dn2}(-t)$ have the same sign and thus add up. This yields the minimum possible value of the MSR:

$$MSR > MSR_{min} = \frac{N}{1 + int\left[\frac{(\frac{N}{2}-1)(N_c-n)}{LCM(N_c-n,N_c+n)}\right]} \quad (10)$$

The value of MSR is also affected by the CC between the carrier waveforms. The maximum CC between carrier waveforms corresponds to identical frequency ranges, thus the CC between carrier waveforms only decreases the sidelobe level and increases the MSR in Eq. (10).

It is also important to estimate the maximum CC between the different GCs as well as the ratio of this CC to the autocorrelation (AC) of the GCs. For instance, the CC between the conventional GC and a concatenated GC is:

$$CC_{g_1 g_n}(t) = g_{A1}(t) * g_{Cn}(-t) + g_{B1}(t) * g_{Dn}(-t) \quad (11)$$

To find the maximum possible value of the CC, we assume all the coefficients of the GCs are equal to one, therefore we neglect the possibility of canceling out by summation. For each set of complementary GCs the maximum CC happens when the maximum number of impulses coincides. Two coincidences are trivial, which occur in the conjunction of two concatenated codes. The two impulses at both sides of the last element of the first code are

located at distances $-(N_c + n)/f_s$ and $(N_c - n)/f_s$ which can readily coincide with any two impulses out of three consecutive impulses of the conventional code with uniform intervals N_c/f_s (Fig. 3(b)).
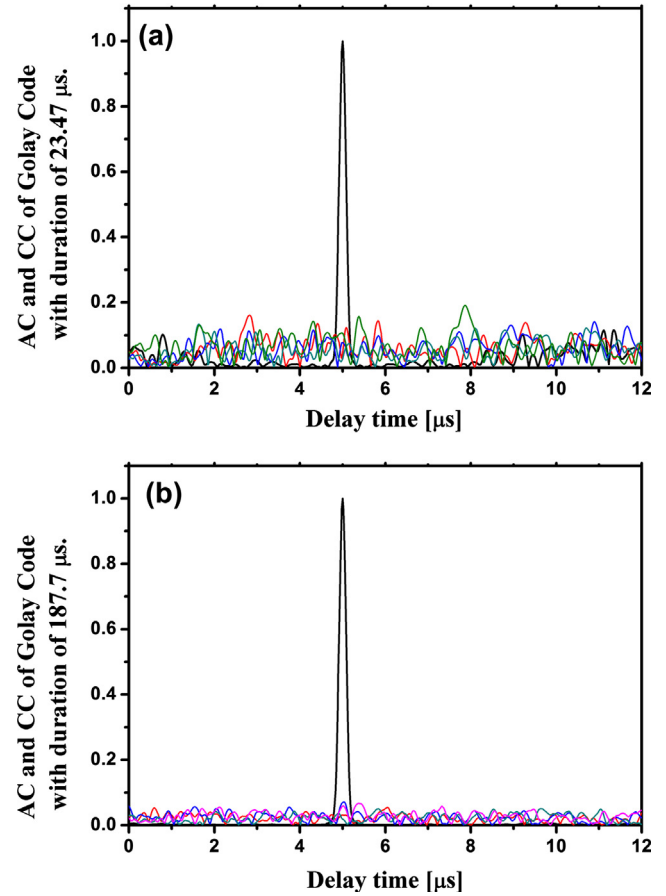
Fig. 4. AC of GC5, as well as CC of GC5 with GC1 to GC4 for signal duration: (a) 23.5 μs and (b) 187.7 μs (simulation).
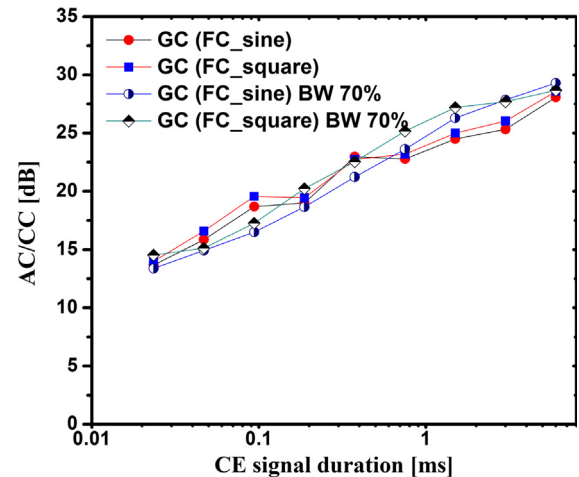
Fig. 5. Increase of the GC5 AC peak to the maximum GC5 CC with GC1 to GC4 (AC/CC) for signal durations from 23.47 μs to 6.007 ms. The simulations were performed for different cases of sinusoidal and square waveforms with and without the transducer effect (70% BW).

Additional coincidences are possible on both sides of the middle impulse, if the codes are long enough to surpass the LCM of intervals of both codes divided by the intervals between impulses in each code, that is:

$$Max[G_{A1}(t) * G_{Cn}(-t)]$$
$$\leqslant \left[2 + \text{int}\left[\frac{(\frac{N}{2}-1)(N_c-n)}{LCM(N_c-n,N_c)} + \frac{(\frac{N}{2}-2)(N_c+n)}{LCM(N_c+n,N_c)}\right]\right]\delta(t-t_i) \quad (12)$$
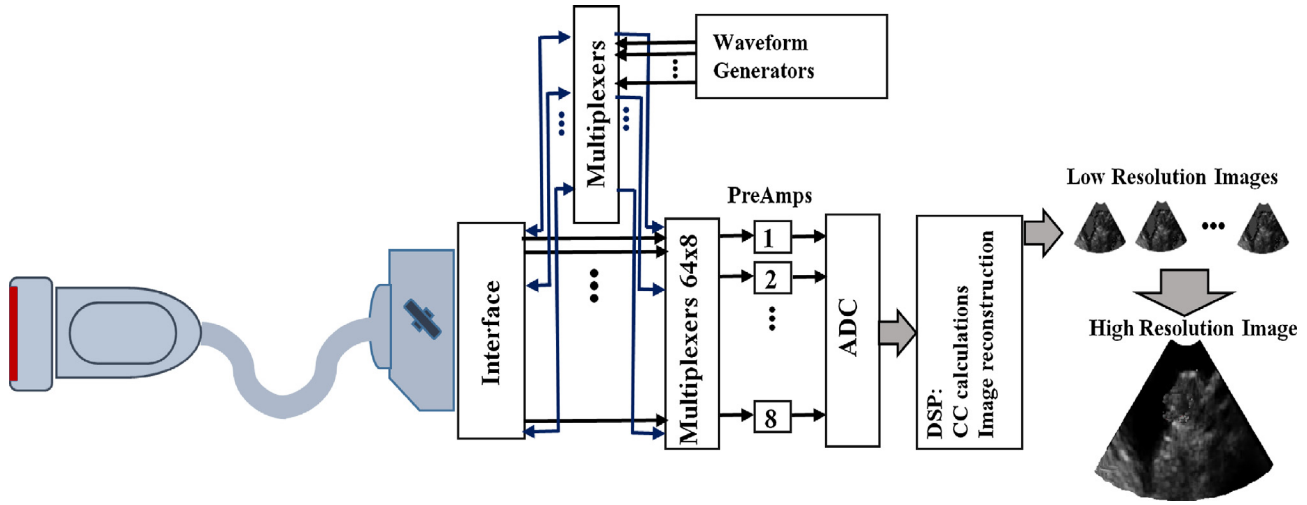
Fig. 6. Schematic diagram of the experimental US imager.
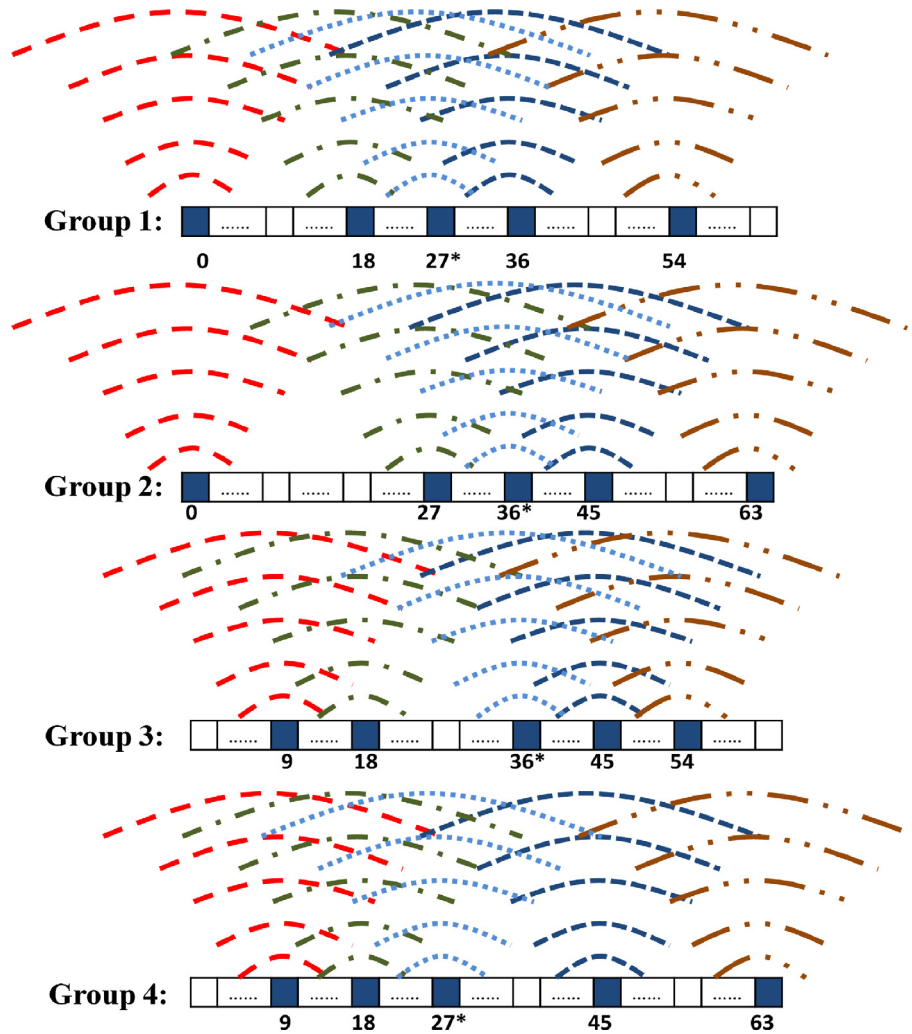
Fig. 7. The schematic for four groups of transmissions, each with five elements at a time. Each FG channel stimulated either of two nearby elements: 0 or 9, 18 or 27, 36 or 45, and 54 or 63. The fifth FG channel was used to stimulated between elements 27 and 36. The element stimulated by the fifth FG channel in each group is marked with '*'.

The following two mathematical identities (a and b are integers) can be used to simplify Eq. (12) [37]:

$$LCM(a,b) = \frac{a \cdot b}{GCF(a,b)} \tag{13a}$$

$$GCF(a,b) = GCF(a-b,b), \quad \text{for } a > b \tag{13b}$$

which yields:

$$\begin{aligned}\frac{(N_c - n)}{LCM(N_c - n, N_c)} &= \frac{GCF(N_c - n, N_c)}{N_c} = \frac{GCF(N_c, n)}{N_c} \\ \frac{(N_c + n)}{LCM(N_c + n, N_c)} &= \frac{GCF(N_c + n, N_c)}{N_c} = \frac{GCF(N_c, n)}{N_c}\end{aligned} \tag{14}$$

Therefore:

$$Max(G_{A1}(t) * G_{Cn}(-t)) \leqslant \left[2 + \text{int}\left[(N-3)\frac{GCF(N_c,n)}{N_c}\right]\right]\delta(t - t_i) \tag{15}$$

The CC of complementary GCs may generate a similar maximum. Therefore AC/CC can be estimated as:

$$\frac{AC}{CC} > \frac{N}{2 + \text{int}\left[(N-3)\frac{GCF(N_c,n)}{N_c}\right]} \tag{16}$$

Similar to the sidelobes of the AC, the CC of the carrier waveform only increases this ratio. Furthermore, by using FC sinusoidal or square carrier waveforms, we can enhance the possibility of sidelobes cancelling each other out and, therefore, both MSR and AC/CC can be enhanced. Simulations in the next section demonstrate that by increasing the code length it is possible to enhance the AC/CC ratio. Experimental results presented in Section 4 are also based on codes as long as 1.5 ms or N = 2048.

2.5. Simulations

Fig. 4(a) and (b) shows the simulated AC of the proposed GC4 as well as its CC with all of the other abovementioned GCs. The signal
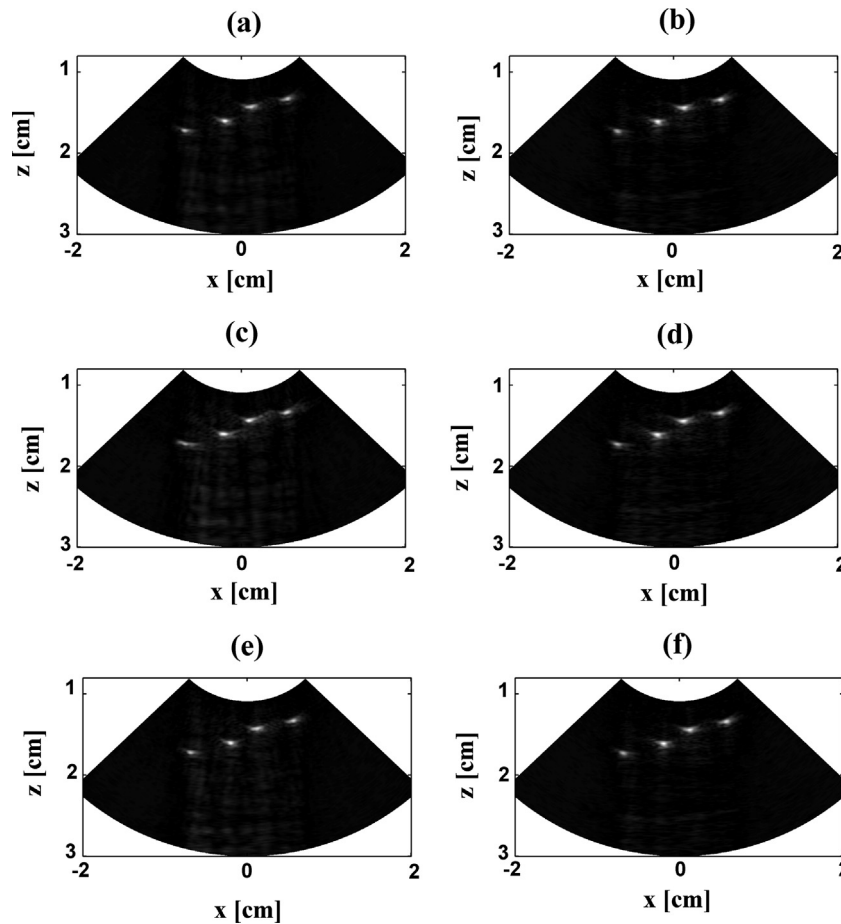
Fig. 8. The images generated with mismatched CEs: (a) sinusoidal FM1 to FM5 (PSNR = 27.8 dB), (b) sinusoidal GC1 to GC5 (PSNR = 32.0 dB), (c) Same image as (a) but with randomly delayed channels (PSNR = 25.8 dB), (d) Same image as (b) but with randomly delayed channels up to 0.5 μs (PSNR = 30.2 dB), The individual signal channels of cases (a) and (b) are added together and the matched filtered with (e) FM1 to FM5 (PSNR = 27.0 dB) and (f) GC1 to GC5 (PSNR = 31.7 dB).

Table 2
The PSNR of images generated with FM and GC (Fig. 8). Also, the FWHM of the axial and lateral section of the third and fourth wires in the images are presented.

	PSNR [dB]	FWHM of axial cross-sections [mm]		FWHM of lateral cross-sections [mm]	
		3rd wire	4th wire	3rd wire	4th wire
(a) FM	27.8	0.51	0.50	0.87	0.87
(b) GC	32.0	0.60	0.53	1.04	0.95
(c) FM + Aberration	25.8	0.48	0.48	1.12	1.67
(d) GC + Aberration	30.2	0.60	0.49	1.33	1.02
(e) FM + Noise	27.0	0.48	0.51	0.86	0.90
(f) GC + Noise	31.7	0.60	0.53	1.04	0.95

durations are 23.47 μs and 187.7 μs for Fig. 4(a) and (b), respectively. The mentioned signal durations are the total duration of two complementary codes which were transmitted with a delay between them. As seen in the figures, a minor CC among the various GC signals exists which is reduced with increasing code duration. A set of simulations were performed for signal duration ranges from 23.47 μs to 6.007 ms and the ratio of the GC4 AC peak to the maximum CC of other GCs with GC4 (AC/CC) is shown in Fig. 5. This figure shows the increase of AC/CC for four cases; sinusoidal carrier, square carrier, without and with consideration of the transducer transfer function (TTF) effect. Here a transducer with CF of 2.7 MHz and 70% fractional bandwidth is considered. All the carrier signals are FC. Again, it is observed that, the maximum AC/CC increases with increasing code duration.

3. The experimental set-up

Fig. 6 shows the diagram of the experimental ultrasound imager. A 64-element phased array was connected to a series of multiplexers through a zero insertion force (ZIF) connection interface. The array transducer SA4-2/24 (Ultrasonix, BC, Canada) had a center frequency of 3 MHz and 78% BW. Eight multiplexer boards (NI PXI-2593, National Instruments, Austin, TX, USA) were employed. At any instant, four of them were used to transfer the receiving signals from the transducer to the acquisition card, a sub-array of 8 transducers. Eight elements of the array were selected and directly connected to the other four multiplexers.

The task of this second set of multiplexers was to switch between the eight elements, thus, at any given time, these 8 selected elements could either perform as transmitters or receivers. Therefore, the multiplexers either connected the selected elements to the receiver multiplexers, or to the function generators. A function generator board (PXI-5442, NI) as well as two dual-channel analog waveform generators (33500B, Agilent Technologies Inc., Santa Clara, California, USA) were used to perform five simultaneous transmissions. The sampling frequency of the waveform generators was set to 30 Ms/s. An 8-channel analog-to-digital converter (PXI-5105, NI) with 60 Ms/s sampling frequency received the detected signals from multiplexers, after amplification (HD28082, 40 dB, HD Communications Corp.). An in-house LabView program was employed to control and synchronize the transmission and acquisition of signals as well as to perform matched filtering. A simple plan could have been to use four transmit elements at a time, thus, in two transmit groups all eight elements could be employed. However, an alternative scheme was used which transmitted from five elements at a time and the transmitting elements were permuted in four groups as demonstrated in Fig. 7. In this scheme, each FG channel stimulated either of two nearby elements: 0 or 9, 18 or 27, 36 or 45, and 54 or 63. The fifth FG channel was used to stimulate elements between 27 and 36. The element stimulated by the fifth FG channel is marked with an asterisk ('*') in the figure. As shown in our previous work [30], using several permutations of transmitting elements can effectively reduce the artifacts generated due to the CC between the codes. This transmission scheme yields 20 low-resolution images with only four transmissions.
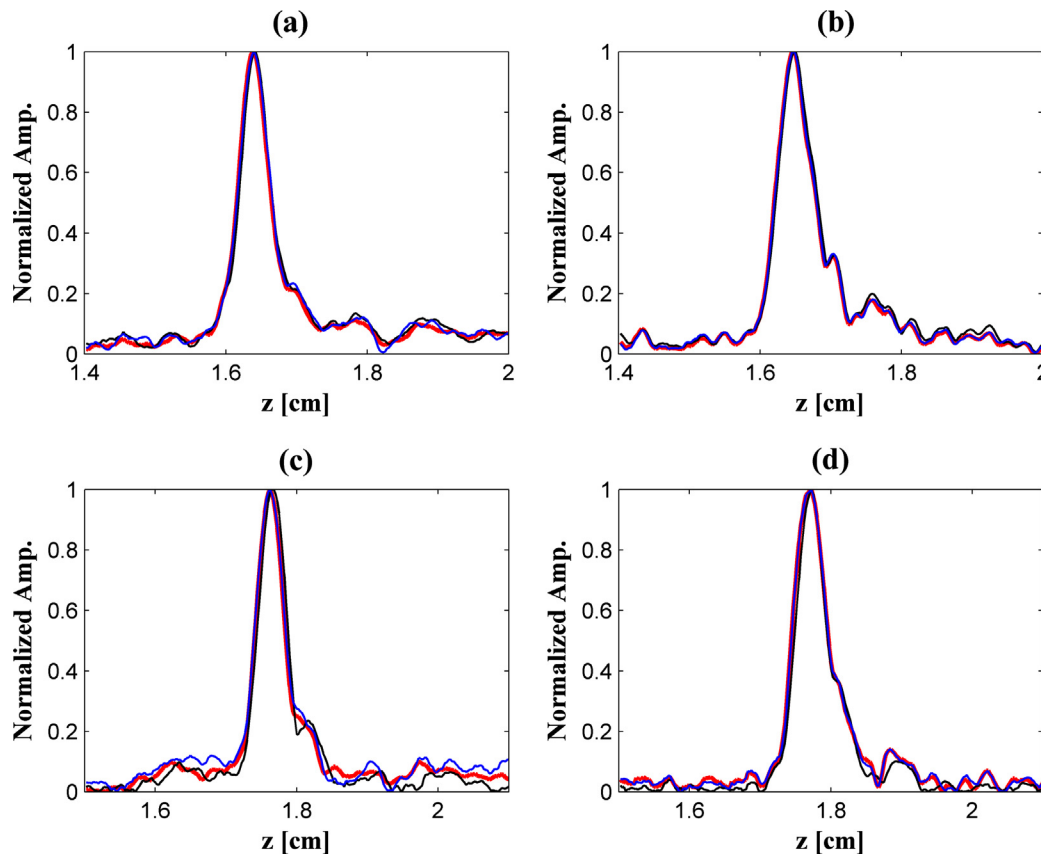
Fig. 9. The axial section of the third and fourth wires from the transducer. The FWHM demonstrates the axial resolution of the image. (a) The third wire section imaged by FM excitation (FWHM = 0.51 mm), (b) the third wire section imaged by GC excitation (FWHM = 0.6 mm), (c) the fourth wire section imaged by FM excitation (FWHM = 0.5 mm), (d) the fourth wire section imaged by GC (FWHM = 0.53 mm). The thick lines (red) correspond to the original images (Fig. 8(a) and (b)), the thin lines correspond to the aberration effect (Fig. 8(c) and (d)), and the normal line (blue) correspond to the noise added data (Fig. 8(e) and (f)). The blue and red lines are very close together and are difficult to distinguish. The FWHM are reported in Table 2 (For interpretation of the references to color in this figure legend, the reader is referred to the web version of this article.).

We used very long coded waveforms to enhance SNR and resolution without switching the transmitter and receiver elements during each signal detection. This greatly reduces the complexity of the system. It should be added that, although in each low resolution image five elements were missing from the receiver, employing four different permutation of transmit elements ensured the use of the full receiving aperture to construct the final image and maintain the spatial resolution. To prevent large cross-talk between the transducer elements saturated due to the detected signal from adjacent elements, very low amplitude signals (20 mV$_{pp}$) were used in transmissions.

4. Experimental results

Ultrasound imaging of four musical instrument wires (0.037″, Malin Co., Cleveland, OH, USA) was performed with the abovementioned set-up to experimentally demonstrate the feasibility of the method. Two different sets of mismatched CEs were tested with the foregoing scheme shown in Fig. 8: (a) The five mismatched sinusoidal chirps corresponding to FM1 to FM5 introduced before: the frequency range of the chirps was between 1.6 to 4.3 MHz and chirp duration was 1.502 ms. (b) the five FC sinusoidal GCs corresponding to GC1 to GC5 in Table 1 with 2048-bit length. The total duration of two complementary GCs was 1.502 ms. It should be added that, in transmitting the GCs, in practice the two parts of the GC were concatenated in one arbitrary waveform file with a delay (~0.1 ms) allocated between the codes. After digitizing the received signal, the LabView program split up the signal into two

parts and calculated each part's pulse compression with the corresponding complementary GC. Then, the two CCs were added to yield the final CC signal. It should be added that in the reconstruction of images coherent summation has been employed. This means that the real and imaginary parts of the signals after matched filtering (the in-phase and quadrature CC) were used in the back-projection algorithm to provide a set of complex values for the final image. The absolute module of these complex values provides the final image. This process significantly improved the contrast and resolution of the final image in comparison to using the envelope signal in the first place to reconstruct the low resolution images. The images in Fig. 8(a) and (b) show the capability of both of the mismatched CEs to generate images of the 4-wire sample. The peak signal-to-noise ratio (PSNR) of each image has been reported in the figure caption as well as Table 2.

To further evaluate the performance of the proposed CEs, a few case studies have been simulated using the same experimental data. In the first case, the effect of phase aberration was examined by adding random time delays to the individual channel signals. Then matched filtering was performed on randomly delayed signals and low resolution images were reconstructed. The employed random delays generated a mean-root-square (rms) aberration strength of 138 ns and a correlation length [38,39] of 1.8 mm. The resulted images are shown in Fig. 8(c) and (d) for FM and GC signals, respectively. It can be seen that the phase aberration reduced the SNR of the images generated by FM and GC excitation (~2 dB).

In the next case, to show the effect of noise interference as well as mismatched properties of the presented families of codes, the
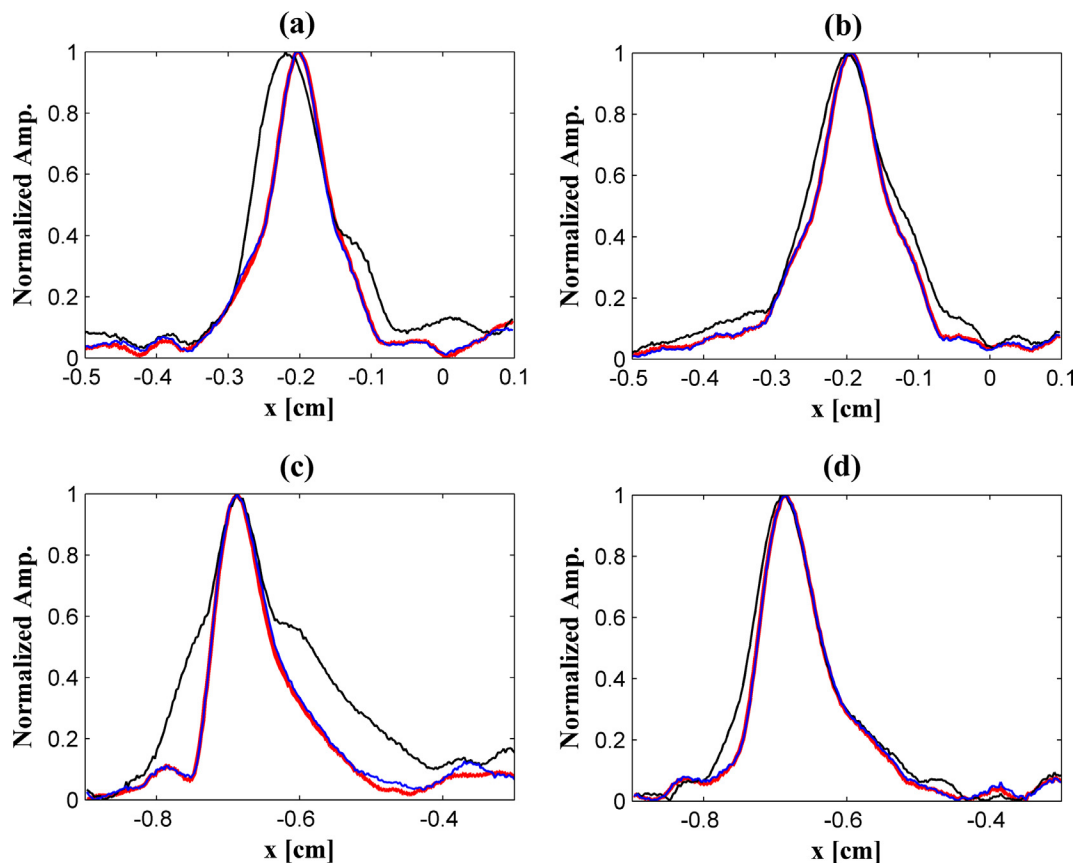
Fig. 10. The lateral section of the third and fourth wires from the transducer. The FWHM demonstrates the lateral resolution of the image. (a) The third wire section imaged by FM excitation (FWHM = 0.87 mm), (b) the third wire section imaged by GC excitation (FWHM = 1.04 mm), (c) the fourth wire section imaged by FM excitation (FWHM = 0.87 mm), (d) the fourth wire section imaged by GC (FWHM = 0.95 mm). The thick lines (here red) correspond to the original images (Fig. 8(a) and (b)), the thin lines correspond to the aberration effect (Fig. 8(c) and (d)), and the normal line (blue) corresponds to the noise added data (Fig. 8(e) and (f)). The blue and red lines are very close together. The FWHM are reported in Table 2 (For interpretation of the references to color in this figure legend, the reader is referred to the web version of this article.).

signals detected in individual channels from both experiments (FM and GC) have been added together to generate a set of mixed signals. In the mixed signals, responses to other CEs simulate the effect of noise in the same frequency range on the other signal. Then the mixed signals were matched filtered with their corresponding family of CEs separately to reconstruct two images (based on FM and GC excitations). The resulted images are shown in Fig. 8(e) and (f). The induced change on the resolution is insignificant and SNR change is minor in both images.

To evaluate the spatial resolution of the images, the axial (depth) cross-sections of the third and fourth wires from the transducer are shown in Fig. 9. Similarly the lateral cross-sections are shown in Fig. 10. The axial resolution and lateral resolution of wire sections has been calculated based on the full-width at half-maximum (FWHM) and reported in the figure captions and Table 2. The FWHM values show comparable resolutions between the two methods with around 15% higher resolution of FM method.

Finally the same sample was imaged with a commercial ultrasonic system (SonixTOUCH, Ultrasonix Medical Corp., Richmond, BC, Canada) and the B-mode image is shown in Fig. 11(a). The B-mode image was generated using the traditional synthetic aperture method (i.e. separate transmits with each transducer element, and receive by the same element) at center frequency of 3.3 MHz. The PSNR of the B-mode image is estimated to be 26 dB. Furthermore,

the cross-section of the wires in Fig. 8(b), the GC image, is co-registered with the wires in the B-mode image and shown in Fig. 11(b). This image demonstrates the higher resolution of CE based SAI compared to the conventional B-mode image created by high voltage pulses and 30 Hz frame rate.

5. Discussion

Fig. 8 shows that, in practice, the new family of mismatched GCs can encode the signals and is as good as mismatched FM chirps. The PSNR of all images are reported in the caption of Fig. 8 and Table 2. Here, the GC method provides higher SNR. The addition of other signals has a minor effect on SNR (>1 dB) and resolution. This shows the robustness of the CE method in the presence of noise which is induced by the very long duration of codes and the wide bandwidth of the receiver. The low correlation between two sets of codes shows the possibility of using both methods together. Dealing with array transducers containing very large number of elements or in pursuing 3D imaging, the availability of such an arsenal of mismatched codes produces a great advantage: All the introduced mismatched codes can be employed together to facilitate multiple transmissions from a large number of elements and generate 3D US images.
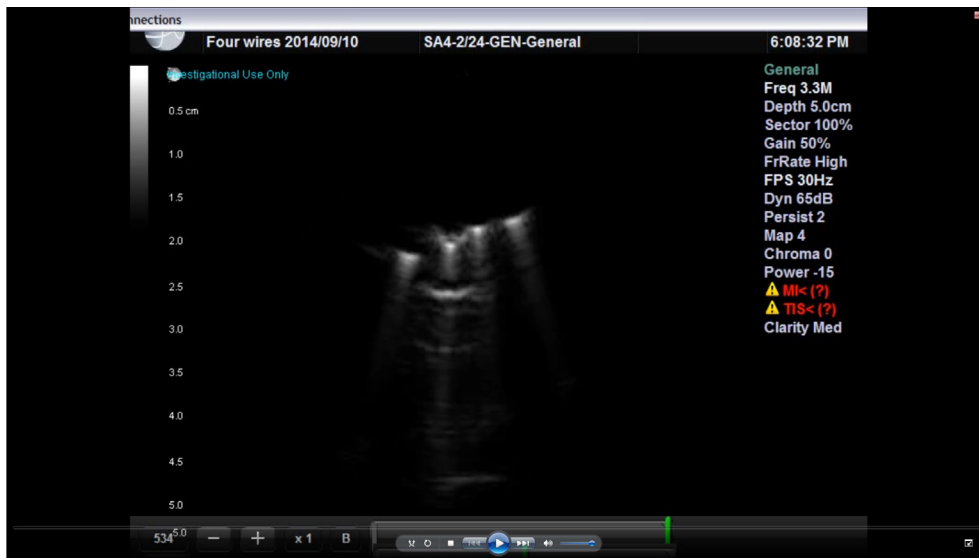
(a)

(b)

Fig. 11. (a) The B-mode image generated by a commercial ultrasonic imager (SonixTOUCH Ultrasonix Medical Corp., Richmond, BC, Canada) (PSNR = 26.5 dB). (b) Co-registered images Fig. 8(b) and B-mode image.

The limitation of concatenating GCs in comparison with FM chirps is that the limited bandwidth of the transducer and the limited sampling frequency can limit the number of effective mismatched codes that can be generated. It is not desirable to have the CF of any part of the concatenating GCs located outside the −6 dB bandwidth of the transducer. In comparison, all of the proposed mismatched FM chirps (Fig. 1(a)) are equally affected by the transducer bandwidth. However, as shown here, five efficient mismatched codes were produced and tested with the sampling frequency of 30 Ms/s, CF of 3 MHz and fractional bandwidth of 78%.

Here, we can compare the frame rate of the proposed scheme with a conventional synthetic aperture imaging where the transmission is performed one at a time. The conventional synthetic aperture method [40] requires eight transmission time intervals for eight elements and would generate eight low-resolution images. The proposed method reduces that acquisition time to half and increases the number of low-resolution images to 20. This can yield higher frame-rate imaging and at the same time superior resolution and depth detectivity. In the presented experiments, every 1.6 ms a set of codes was transmitted (PRF = 625 Hz) and each image was generated from four measurements (20 CEs). Therefore, considering the acquisition time, the new system is capable of performing imaging with a frame rate of 156.25 Hz.

The use of CE and SAI requires additional processing time for pulse compression as well as image reconstruction. This is contrary to the main objective of the study which is high-frame-rate imaging. To justify the use of these methods, we should mention that new trends in using field-programmable gate arrays (FPGA) and graphic processing units (GPU) facilitate efficient parallel processing of the US imaging workflow [41–43]. These emerging digital technologies are essential for realizing high-frame-rate US imaging.

Another issue that may arise from using CW excitation, is the thermal effect of ultrasound. Overheating can cause damage to both piezoelectric element and the interrogated tissue. The total average power and duty cycle should be limited to the manufacturer's recommendation to prevent overheating and depoling the piezoelectric crystal. Furthermore, the thermal index at the transducer surface and focal distance should be kept according to the safety recommendations [44–46]. In the present experiments the very small input voltage (20 mV) to the piezoelements and duty cycle due to permutation of transmit elements, induced extremely low acoustic intensity and therefore was far too low to cause any of the abovementioned problems.

In this work, similar to our previous paper [30], the focus was on ultrasound imaging. However, there are similar applications in other fields such as sonar, radar, and wireless communications with multiple antennas where the use of mismatched codes facilitates simultaneous multiple transmitting and receiving. The results presented here can be readily applied in those fields due to the similarity of their signal processing methods. One related modality is photoacoustics (PA). Photoacoustic has a unique synergy with, and similarity to, ultrasound imaging, due to the optical-to-ultrasound energy conversion phenomenon, the detection process and image reconstruction. The co-registration of these two modalities can enrich the anatomical and physiological information that each modality can provide separately [41,43,47]. It has been shown that the application of CE in Photoacoustic can offer more than enhanced SNR: Frequency-domain (FD) Photoacoustic offers some techniques that can enhance the sensitivity and specificity of tissue characterization. Techniques such as wavelength-modulated differential spectroscopy and phase spectroscopy are examples of FD Photoacoustic features [48,49]. A major advantage the use of mismatched CE can provide for Photoacoustic spectroscopy is to reduce the errors caused by biological motions like breathing. Use of simultaneous laser irradiation and possibility of decoding of the responses eliminate deviation of signals due to such motions. Previously, we showed the use of mismatched FM chirps for simultaneous Photoacoustic spectroscopy [50]. The mismatched codes presented in this paper can also be employed for simultaneous Photoacoustic imaging with multiple wavelengths.

6. Conclusions

The objective of this study was to generate multiple mismatched CEs. The weak correlations among these codes facilitate simultaneous multiple transmission and separation of the responses in the receiver. In this paper, a new method for generating an arbitrary number of mismatched codes was presented. The new method employs concatenated GCs with different carrier frequencies to produce multiple mismatched GCs. The application of this new family of mismatched codes along with mismatched FM chirps was demonstrated experimentally. Both methods are shown to be capable of encoding the multiple transmitted signals and decoding the received responses. One of the advantages of the presented codes is that they are based on Golay sequences. The use of orthogonal GCs for simultaneous insonification has been described before [18,19]. Two orthogonal GCs are readily available. However, the challenge was in generating multiple orthogonal sequences. By concatenating the GC parts for each orthogonal code, automatically a set of new mismatched codes are created. Therefore, the number of mismatched codes can easily increase by a factor of two.

In a conventional ultrasound imaging, a line image, and in classical synthetic aperture imaging, a low-resolution image is generated one at a time. The ability of encoding the transmitted signals and simultaneous insonification enables high-frame-rate ultrasound imaging. In the presented experiments, five concurrent mismatched codes were employed each time. Every code independently yielded its own image due to an unfocused insonification. Therefore, the use of mismatched codes increased the signal acquisition rate by five times. However, to reduce the artifacts in the images caused by CCs among the mismatched codes, different combination of elements and codes were employed in the transmit mode. Combining all the images yields an image with fewer artifacts. Although the averaging process compromises the frame rate, it was shown that the benefit of multiple simultaneous insonifications surpasses the extra time required for multiple signal detection for the sake of averaging. Therefore, the method is capable of decreasing the total acquisition time and enhancing the frame rate. The major advantage of the presented mismatched CEs over BW division methods is that they share the same signal duration and bandwidth, thereby producing uniform resolution and SNR during the image generation process.

References

[1] R. Cobbold, Foundations of Biomedical Ultrasound, Oxford University Press, 2007.
[2] D.P. Shattuck, M.D. Weinshenker, S.W. Smith, O.T. von Ramm, Explososcan: a parallel processing technique for high speed ultrasound imaging with linear phased arrays, J. Acoust. Soc. Am. 75 (4) (1984) 1273–1282.
[3] O.T. von Ramm, S.W. Smith, H.G. Pavy, High-speed ultrasound volumetric imaging system—Part II: Parallel processing and image display, IEEE Trans. Ultrason. Ferroelectr. Freq. Contr. 38 (2) (1991) 109–115.
[4] T. Hergum, T. Bjastad, K. Kristoffersen, H. Torp, Parallel beamforming using synthetic transmit beams, IEEE Trans. Ultrason. Ferroelectr. Freq. Contr. 54 (2) (2007) 271–280.

[5] G.R. Bredthauer, O.T. von Ramm, Array design for ultrasound imaging with simultaneous beams, in: IEEE Int. Symp. Biomedical Imaging, Washington D.C., 2002.

[6] G. Montaldo, M. Tanter, J. Bercoff, N. Benech, M. Fink, Coherent plane-wave compounding for very high frame rate ultrasonography and transient elastography, IEEE Trans. Ultrason. Ferroelectr. Freq. Contr. 56 (3) (2009) 489–506.

[7] J.-L. Gennisson, M. Renier, S. Catheline, C. Barriere, J. Bercoff, M. Tanter, M. Fink, Acoustoelasticity in soft solids: assessment of the nonlinear shear modulus with the acoustic radiation force, J. Acoust. Soc. Am. 122 (6) (2007) 3211–3219.

[8] J.A. Jensen, S.I. Nikolov, K.L. Gammelmark, M.H. Pedersen, Synthetic aperture ultrasound imaging, Ultrason. J. 44 (2006) e5–e15.

[9] M. Karaman, P.-C. Li, M. O'Donnell, Synthetic aperture imaging for small scale systems, IEEE Trans. Ultrason. Ferroelectr. Freq. Contr. 42 (1995) 429–442.

[10] M. O'Donnell, Y. Wang, Coded excitation for synthetic aperture ultrasound imaging, IEEE Trans. Ultrason. Ferroelectr. Freq. Contr. 52 (2) (2005) 171–176.

[11] I. Trots, Y. Tasinkevych, A. Nowicki, M. Lewandowski, Golay coded sequence in synthetic aperture imaging systems, Arch. Acoust. 36 (4) (2011) 913–926, http://dx.doi.org/10.2478/v10168-011-0061-5.

[12] M.F. Rasmussen, J.A. Jensen, Comparison of 3-D synthetic aperture phased-array ultrasound imaging and parallel beamforming, IEEE Trans. Ultrason. Ferroelectr. Freq. Contr. 61 (10) (2014) 1638–1650.

[13] P. Karwat, Z. Klimonda, M. Lewandowski, A. Nowicki, Imaging quality of the classical beamforming, SAFT and plane wave imaging – experimental results, in: IEEEInternational Ultrasonics Symposium (IUS), 2012, 2012, pp. 1–4.

[14] M.K. Kiymik, I. Gűler, O. Hasekioglub, M. Karaman, Ultrasound imaging based on multiple beamforming with coded excitation, Sign. Process. 58 (1997) 107–113.

[15] J. Shen, E.S. Ebbini, A new coded-excitation ultrasound imaging system—Part I: Basic principles, IEEE Trans. Ultrason. Ferroelectr. Freq. Contr. 43 (1996) 131–140.

[16] M. Golay, Complementary series, IRE Trans. Inform. Theory IT 7 (1961) 82–87.

[17] B.B. Lee, E.S. Furgason, Golay codes for simultaneous multi-mode operation in phased arrays, in: Ultrasonics Symposium, 1982, pp. 821–825.

[18] J.S. Hwang, T.K. Song, Ultrasound Imaging Apparatus and Method using Golay Codes with Orthogonal Property, US Pat. 6547733 B2, 2003.

[19] R.Y. Chiao, L.J. Thomas, Method and Apparatus for Ultrasonic Synthetic Transmit Aperture Imaging using Orthogonal Complementary Codes, U.S. Patent 6,048,315, 2000.

[20] R.Y. Chiao, L.J. Thomas, Synthetic transmit aperture imaging using orthogonal Golay coded excitation, in: Proc. IEEE Ultrason. Symp., 2000, pp. 1677–1680.

[21] M. Yang, C. Chakrabarti, Design of orthogonal coded excitation for synthetic aperture imaging in ultrasound systems, in: IEEE International Symposium on Circuits and Systems (ISCAS), 2012, pp. 113–116.

[22] T. Misaridis, J.A. Jensen, Space-time encoding for high frame rate ultrasound imaging, Ultrason. J. 40 (2002) 593–597.

[23] P. Gong, M.C. Kolios, Y. Xu, Delay-encoded transmission and image reconstruction method in synthetic transmit aperture imaging, IEEE Trans. Ultrason. Ferroelectr. Freq. Contr. 62 (10) (2015) 1745–1755.

[24] T. Misaridis, J.A. Jensen, Use of modulated excitation signals in medical ultrasound, Part III: High frame rate imaging, IEEE Trans. Ultrason. Ferroelectr. Freq. Contr. 52 (2) (2005) 207–218.

[25] F. Gran, J.A. Jensen, Spatio-temporal encoding using narrow-band linear frequency modulated signals in synthetic ultrasound imaging, SPIE Proc. Progress in Biomedical Optics and Imaging, vol. 5750, 2005, pp. 405–416.

[26] V. Behar, D. Adam, Optimization of sparse synthetic transmit aperture imaging with coded excitation and frequency division, Ultrason. J. 43 (2005) 777–788.

[27] F. Gran, J.A. Jensen, Frequency division transmission imaging and synthetic aperture reconstruction, IEEE Trans. Ultrason. Ferroelectr. Freq. Contr. 53 (5) (2006) 900–911.

[28] A. Wegner, Spread Spectrum Coded Waveforms in Ultrasound Imaging, US Patent 8939909 B2, 27 01, 2005.

[29] T.K. Song, Y.K. Jeong, Ultrasound Imaging System and Method based on Simultaneous Multiple Transmit-focusing using Weighted Orthogonal Chirp Signals, U.S. Patent 7066886 B2, 2006.

[30] B. Lashkari, K. Zhang, A. Mandelis, High frame rate synthetic aperture ultrasound imaging using mismatched coded excitation waveform engineering: a feasibility study, IEEE Trans. Ultrason. Ferroelectr. Freq. Contr. 63 (6) (2016) 828–841.

[31] N. Levanon, E. Mozeson, Radar Signals, second ed., John Wiley & Sons, New Jersey, 2004.

[32] M. O'Donnell, Coded excitation system for improving the penetration of real-time phased-array imaging systems, IEEE Trans. Ultrason. Ferroelectr. Freq. Contr. 39 (3) (1992) 341–351.

[33] C.E. Cook, M. Bernfeld, Radar Signals: An Introduction to Theory and Application, Academic Press, New York, 1967.

[34] S.Z. Budisin, New complementary pairs of sequences, Electron. Lett. 26 (13) (1990) 881–883.

[35] D.Z. Dokovic, Equivalence classes and representatives of Golay sequences, Discr. Math. 189 (1998) 79–93.

[36] A. Nowicki, I. Trots, P.A. Lewin, W. Secomski, R. Tymkiewicz, Influence of the ultrasound transducer bandwidth on selection of the complementary Golay bit code length, Ultrason. J. 47 (2007) 64–73.

[37] R.A. Mollin, Algebraic Number Theory, second ed., CRC Press, Boca Raton, FL, 2011, p. 30.

[38] L.M. Hinkelman, T.L. Szabo, R.C. Waag, Measurements of ultrasonic pulse distortion produced by human chest wall, J. Acoust. Soc. Am. 101 (4) (1997) 2365–2373.

[39] J.J. Dahl, D.A. Guenther, G.E. Trahey, Adaptive imaging and spatial compounding in the presence of aberration, IEEE Trans. Ultrason. Ferroelectr. Freq. Contr. 52 (7) (2005) 1131–1144.

[40] J.A. Johnson, M. Karaman, B.T. Khuri-Yakub, Coherent-array imaging using phased subarray. Part I: Basic principles, IEEE Trans. Ultrason. Ferroelectr. Freq. Contr. 52 (1) (2005) 37–50.

[41] U. Alqasemi, Li. Hai, A. Aguirre, Q. Zhu, FPGA-based reconfigurable processor for ultrafast interlaced ultrasound and photoacoustic imaging, IEEE Trans. Ultrason. Ferroelectr. Freq. Contr. 59 (7) (2012) 1344–1353.

[42] C.C.P. Cheung, A.C.H. Yu, N. Salimi, B.Y.S. Yiu, I.K.H. Tsang, B. Kerby, R. Zahiri Azar, K. Dickie, Multi-channel pre-beamformed data acquisition system for research on advanced ultrasound imaging methods, IEEE Trans. Ultrason. Ferroelectr. Freq. Contr. 59 (2) (2012) 243–253.

[43] J. Yuan, G. Xu, Y. Yu, Y. Zhou, P.L. Carson, X. Wang, X. Liu, Real-time photoacoustic and ultrasound dual-modality imaging system facilitated with graphics processing unit and code parallel optimization, J. Biomed. Opt. 18 (8) (2013) 86001–86005.

[44] J. Abbott, Rationale and derivation of MI and TI: a review, Ultrasound Med. Biol. 25 (1999) 431–441.

[45] S.B. Barnett, G.R. Ter Haar, M.C. Ziskin, H.D. Rott, F.A. Duck, K. Maeda, International recommendations and guidelines for the safe use of diagnostic ultrasound in medicine, Ultrasound Med. Biol. 26 (3) (2000) 355–366.

[46] T.A. Bigelow, C.C. Church, K. Sandstorm, J.G. Abbott, M.C. Ziskin, P.D. Edmounds, B. Herman, K.E. Thomenius, T.J. Teo, The thermal index, J. Ultrasound Med. 30 (2011) 714–734.

[47] E. Dovlo, B. Lashkari, A. Mandelis, W. Shi, F.-F. Liu, Photoacoustic radar phase-filtered spatial resolution and co-registered ultrasound image enhancement for tumor detection, Biomed. Opt. Express 6 (3) (2015) 1003–1009.

[48] S.S.S. Choi, B. Lashkari, E. Dovlo, A. Mandelis, Wavelength-modulated differential photoacoustic radar imager (WM-DPARI): accurate monitoring of absolute hemoglobin oxygen saturation, Biomed. Opt. Express 7 (7) (2016) 2586–2596.

[49] B. Lashkari, S.S. Choi, E. Dovlo, S. Dhody, A. Mandelis, Frequency-domain photoacoustic phase spectroscopy: a fluence-independent approach for quantitative probing of hemoglobin oxygen saturation, IEEE J. Sel. Top. Quantum Electron. 22 (3) (2016) 1–10.

[50] B. Lashkari, S.S. Choi, M.E. Khosroshahi, E. Dovlo, A. Mandelis, Simultaneous dual-wavelength photoacoustic radar imaging using waveform engineering with mismatched frequency modulated excitation, Opt. Lett. 40 (7) (2015) 1145–1148.